Negative and positive feedback from a supernova remnant with SHREC. a detailed study of the shocked gas in IC443

Monthly Notices of the ROYAL ASTRONOMICAL SOCIETY

MNRAS **511,** 953–963 (2022) https://doi.org/10.1093/mnras/stac070
Advance Access publication 2022 January 12

Negative and positive feedback from a supernova remnant with SHREC: a detailed study of the shocked gas in IC443

G. Cosentino [1]★ I. Jiménez-Serra,[2] J. C. Tan,[1,3] J. D. Henshaw [4] A. T. Barnes [5] C.-Y. Law,[1,6] S. Zeng [7] F. Fontani [8] P. Caselli,[9] S. Viti,[10,11] S. Zahorecz,[12,13] F. Rico-Villas,[2] A. Megías [2] M. Miceli,[14,15] S. Orlando,[15] S. Ustamujic,[15] E. Greco,[15,16,17] G. Peres,[14,15] F. Bocchino [15] R. Fedriani,[1] P. Gorai,[1] L. Testi[6] and J. Martín-Pintado[2]

[1]*Space, Earth and Environment Department, Chalmers University of Technology, SE-412 96 Gothenburg, Sweden*
[2]*Centro de Astrobiología (CSIC/INTA), Ctra. de Torrejón a Ajalvir km 4, E-28850 Madrid, Spain*
[3]*Department of Astronomy, University of Virginia, 530 McCormick Road Charlottesville, VA 22904, USA*
[4]*Max Planck Institute for Astronomy, Königstuhl 17, D-69117 Heidelberg, Germany*
[5]*Argelander-Institut für Astronomie, Universität Bonn, Auf dem Hügel 71, D-53121 Bonn, Germany*
[6]*European Southern Observatory, Karl-Schwarzschild-Strasse 2, D-85748 Garching, Germany*
[7]*Star and Planet Formation Laboratory, Cluster for Pioneering Research, RIKEN, 2-1 Hirosawa, Wako, Saitama, 351-0198, Japan*
[8]*INAF Osservatorio Astronomico di Arcetri, Largo E. Fermi 5, I-50125 Florence, Italy*
[9]*Max Planck Institute for Extraterrestrial Physics, Giessenbachstrasse 1, D-85748 Garching bei München, Germany*
[10]*Leiden Observatory, Leiden University, PO Box 9513, NL-2300 RA Leiden, The Netherlands*
[11]*Department of Physics and Astronomy, University College London, Gower Street, London WC1E 6BT, UK*
[12]*Department of Physical Science, Graduate School of Science, Osaka Prefecture University, 1-1 Gakuen-cho, Naka-ku, Sakai, Osaka 599-8531, Japan*
[13]*National Astronomical Observatory of Japan, National Institutes of Natural Science, 2-21-1 Osawa, Mitaka, Tokyo 181-8588, Japan*
[14]*Dipartimento di Fisica e Chimica E. Segrè, Università di Palermo, Via Archirafi 36, I-90123 Palermo, Italy*
[15]*INAF, Osservatorio Astronomico di Palermo, Piazza del Parlamento 1, I-90134 Palermo, Italy*
[16]*Anton Pannekoek Institute for Astronomy, University of Amsterdam, Science Park 904, NL-1098 XH Amsterdam, The Netherlands*
[17]*GRAPPA, University of Amsterdam, Science Park 904, NL-1098 XH Amsterdam, The Netherlands*

Accepted 2021 December 21. Received 2021 December 3; in original form 2021 October 14

ABSTRACT

Supernova remnants (SNRs) contribute to regulate the star formation efficiency and evolution of galaxies. As they expand into the interstellar medium (ISM), they transfer vast amounts of energy and momentum that displace, compress, and heat the surrounding material. Despite the extensive work in galaxy evolution models, it remains to be observationally validated to what extent the molecular ISM is affected by the interaction with SNRs. We use the first results of the ESO–ARO Public Spectroscopic Survey SHREC to investigate the shock interaction between the SNR IC443 and the nearby molecular clump G. We use high-sensitivity SiO(2-1) and $H^{13}CO^+$(1-0) maps obtained by SHREC together with SiO(1-0) observations obtained with the 40-m telescope at the Yebes Observatory. We find that the bulk of the SiO emission is arising from the ongoing shock interaction between IC443 and clump G. The shocked gas shows a well-ordered kinematic structure, with velocities blue-shifted with respect to the central velocity of the SNR, similar to what observed towards other SNR–cloud interaction sites. The shock compression enhances the molecular gas density, $n(H_2)$, up to $>10^5$ cm^{-3}, a factor of >10 higher than the ambient gas density and similar to values required to ignite star formation. Finally, we estimate that up to 50 per cent of the momentum injected by IC443 is transferred to the interacting molecular material. Therefore, the molecular ISM may represent an important momentum carrier in sites of SNR–cloud interactions.

Key words: ISM: clouds – ISM: individual objects: IC443, clump G – ISM: kinematics and dynamics – ISM: supernova remnants.

1 INTRODUCTION

Massive stars ($M \geq 8$ M$_\odot$) drive powerful stellar feedback that profoundly affects the evolution and star formation efficiency (SFE) of the hosting galaxies. Of such mechanisms, feedback driven by supernova explosions (SNe) is among the most energetic (Bally 2011) and long-lasting (e.g. Leitherer et al. 1999; Agertz et al. 2013). As the remnant expands, the hot plasma pushes and compresses outwards the atomic and molecular gas in contact with the remnant (Chevalier 1974) and injects energy, mass, and momentum into the interstellar medium (ISM), profoundly affecting its physical properties at multiple spatial scales (see Slane et al. 2016, for a review). Mass, energy, and momentum are transferred to the

★ E-mail: giuliana.cosentino@chalmers.se

nearby material during the adiabatic phase, also known as Sedov–Taylor phase (Taylor 1950; Sedov 1959), during which the energy dissipation is due to expansion and radiative losses are negligible (Chevalier 1974; Cioffi, McKee & Bertschinger 1988; Blondin et al. 1998; Kim & Ostriker 2015; Martizzi, Faucher-Giguère & Quataert 2015).

At galactic scales, supernova remnants (SNRs) drive mass-loaded winds that can displace the molecular material, delaying its conversion into stars and hence suppressing star formation in galaxies (Bigiel et al. 2008, 2010; Krumholz, Dekel & McKee 2012; Leroy et al. 2013). This is known as *negative feedback* (Körtgen et al. 2016; Kruijssen et al. 2019). At the same time, the shock compression of surrounding molecular gas by expanding SNRs can locally (spatial scales <10 pc) enhance the density of the molecular material, increase the gas turbulence, and eventually trigger the formation of new stars (Inutsuka et al. 2015; Klessen & Glover 2016). This effect is known as *positive feedback*. The interplay and relative dominance between positive and negative feedback may depend on several conditions, e.g. the density and gas distribution of the processed material, the evolutionary stage of SNRs (Shima, Tasker & Habe 2017), and it is paramount in regulating the SFE and time evolution of galaxies (Bigiel et al. 2008, 2010; Scannapieco et al. 2008; Leroy et al. 2013; Heckman & Thompson 2017). Indeed, it is essential to include stellar feedback in numerical simulations of galactic disc evolution to predict star formation rate and stellar masses comparable to those measured in the ISM (Hennebelle & Iffrig 2014; Smith, Sijacki & Shen 2018; Marinacci et al. 2019).

Over time, galaxy evolution simulations have adopted different ad hoc approaches to include SNRs feedback. Early low spatial resolution models treated SN feedback by manually injecting energy into the system at once (for an overview, see Ceverino & Klypin 2009). Such an approach did not consider the Sedov–Taylor phase and as a result, all the injected energy was quickly radiated away with no effects on the ISM (Katz 1992). In order to overcome this problem and force the adiabatic phase to occur, later works introduced an artificial delay in the radiative cooling, either by redistributing the injected energy both in space and time (Dalla Vecchia & Schaye 2012) or by switching it off for a certain length of time (Stinson et al. 2006; Governato et al. 2010; Agertz, Teyssier & Moore 2011; Teyssier et al. 2013). Alternatively to these 'delaying cooling' methods, other works treat SN feedback as mechanical feedback and introduce the SNRs at a certain time, with a certain radius and by turning on their kinetic energy and momentum in an ad hoc manner (Dubois & Teyssier 2008; Kimm & Cen 2014; Martizzi et al. 2016). Recent high-resolution simulations within the Feedback In Realistic Environments (FIRE) project are in the process of implementing self-consistently the treatment of SN feedback in galaxy evolution models (e.g. Wetzel et al. 2016; Sanderson et al. 2018). These works resolve in space and time the different SN evolutionary stages and the different structures of the ISM, limiting the use of sub-resolution approximations for feedback processes (Hopkins et al. 2014). Finally, extensive theoretical studies focused on the impact of SN-driven feedback on to the dense molecular material of the ISM have been reported by, e.g. Padoan et al. (2016), Padoan et al. (2017), and Seifried et al. (2020).

In light of all these extensive theoretical works, current models are able to efficiently describe the expansion of SNRs in a single and/or multiphase ISM and to make predictions on the energy and momentum imprinted on the nearby material (Koo et al. 2020). However, such predictions are still to be fully validated from an observational point of view. In particular, it remains to be constrained the amount of momentum and energy injected by SNRs into the molecular phase of the ISM, i.e. the material that primarily fuels star formation in galaxies. This can be efficiently done by studying the emission of those molecular species that trace the high-density shocked gas and whose mm and sub-mm emission is enhanced in sites of SNR–cloud interactions (e.g. Neufeld et al. 2007). Among these species, silicon monoxide (SiO) is a unique tracer of dense and shocked molecular material (critical density $n_{crit} > 10^5$ cm^{-3}). Indeed, SiO appears heavily depleted in quiescent regions ($\chi \sim 10^{-12}$; Martin-Pintado, Bachiller & Fuente 1992; Jiménez-Serra et al. 2005) but its abundances can be enhanced by up to a factor of $\sim 10^6$ in regions where the shock propagation causes the sputtering of dust grains or grain–grain collisions. Here, Si is released into the gas phase and SiO is quickly formed (Caselli, Hartquist & Havnes 1997; Schilke et al. 1997; Gusdorf et al. 2008; Jiménez-Serra et al. 2008). SiO emission triggered by SNR shocks has been detected towards W51 (Dumas et al. 2014) and W28 (Vaupre 2015), as part of multiline studies aimed to infer cosmic ray enhancement in SNRs. More recently, in Cosentino et al. (2019), we have reported a dedicated study of the SiO emission arising from the shock interaction between the SNR W44 and the molecular cloud G034.77-00.55 (thereafter G034). Towards this source, the molecular gas pushed away by the expansion of the SNR is interacting with the preexisting massive molecular cloud, causing a parsec-scale shock seen with relatively narrow SiO emission (<3 km s^{-1}). The shock is propagating at a velocity of $\sim$23 km s^{-1} and is compressing the gas to densities $n(H_2) > 10^5$ cm^{-3} (Cosentino et al. 2019). The momentum injected into the dense shocked gas is estimated to be $\sim$20 $M_\odot$ km s^{-1} (Cosentino et al. 2019).

In order to extend the literature sample of SNR–cloud interaction sites seen in SiO emission, we have initiated the ESO–ARO Public Spectroscopic Survey 'SHock interactions between supernova REmnants and molecular Clouds', i.e. SHREC, an ongoing large (800 h) observing program using the 12-m antenna at the Arizona Radio Observatory (ARO). SHREC aims to identify sites of ongoing SNR–cloud interaction by mapping the SiO(2-1), $H^{13}CO^+$(1-0), and $HN^{13}C$(1-0) emission towards a sample of 27 SNRs. These sources have been selected for being relatively nearby (kinematic distance $\leq$ 6 kpc) and for showing evidence of interaction with the surrounding molecular material (Ferrand & Safi-Harb 2012; Green 2019). This includes enhanced X-ray emission, the presence of OH maser emission at 1720 MHz, and enhanced CO(2-1)/CO(1-0) ratios (Slane et al. 2016). The final goal of SHREC is to identify sites of large-scale interactions driven by SNRs and to investigate how these affect the star formation potential and dispersal of the surrounding molecular material. The technical presentation of the project and first data release will be presented in a forthcoming paper (Cosentino et al., in preparation).

1.1 The SNR IC443

As part of SHREC, we have obtained SiO(2-1) and $H^{13}CO^+$(1-0) emission maps towards the well-known source G189.1+3.0, also known as IC443. IC443 is a mixed-morphology SNR, i.e. with a shell-like morphology in the radio wavelengths and centrally filled in the X-rays (Rho & Petre 1998). The source is located at a distance of $\sim$1.9 kpc (Ambrocio-Cruz et al. 2017) and its age estimate is highly uncertain. Although a typical age of $\sim$30 000 yr is usually assumed (Chevalier 1999), recent simulations suggest that the SNR could be much younger ,i.e. $\sim$3000–8000 yr (Troja et al. 2008; Ustamujic et al. 2021).

The IC443 shell is known to be expanding into an atomic cloud in the north-east (Denoyer 1979) and into a molecular cloud in the north-

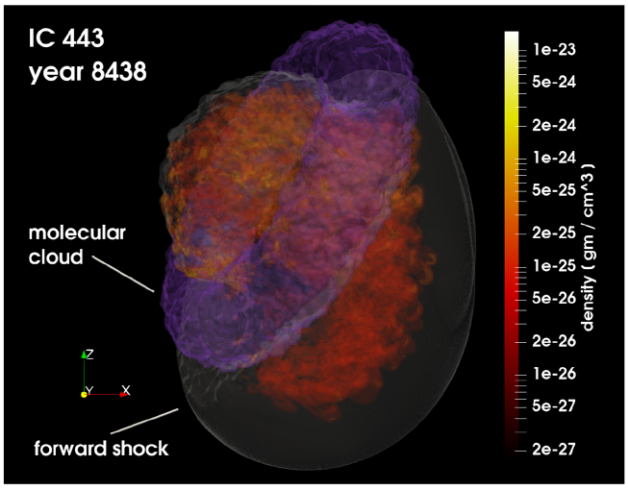

Figure 1. Three-dimensional structure of IC443 derived with a hydrodynamic model that reproduces the morphology of the remnant and the distribution of ejecta (Ustamujic et al. 2021). The volume rendering that uses the red colour palette (colour coding on the right of the panel) shows the distribution of ejecta approximately 8400 yr after the supernova explosion. The semitransparent grey outer surface marks the position of the forward shock. The semitransparent toroidal structure in purple represents the molecular cloud with which the blast wave of the remnant is interacting. The Earth vantage point lies on the negative *y*-axis, i.e. the perspective is in the plane of the sky.

west to south-east direction (Cornett, Chin & Knapp 1977). The first map of the giant molecular cloud surrounding the SNR was reported by Cornett et al. (1977) by means of CO(1-0) emission. Later on, Denoyer (1979) and Huang & Thaddeus (1986) identified four major sites of interaction between IC443 and the cloud, named clumps A, B, C, and G. By using *XMM–Newton* maps of the X-ray emission associated with the SNR, Troja, Bocchino & Reale (2006) reported a geometry of the SNR–cloud system consistent with that of a toroidal molecular cloud wrapped around the expanding SNR and tilted by $\sim 50^\circ$ with respect to the equatorial mid-plane. The three-dimensional structure of the cloud–SNR system is reported in Fig. 1, as derived with the hydrodynamic model presented by Ustamujic et al. (2021). In the geometry presented in Fig. 1, clump G corresponds to the part of the torus that is located in the foreground, between the observer and the expanding shell. Among the identified sites, clump G shows the strongest evidence of ongoing shock interaction, i.e. the presence of OH maser emission (e.g. Hewitt et al. 2006), shocked material probed by multitransitions CO gas (e.g. Zhang, Gao & Wang 2010; Dell'Ova et al. 2020), localized non-thermal X-ray emission (e.g. Petre et al. 1988; Bocchino & Bykov 2000), and shock-excited H_2 emission (e.g. Reach et al. 2019). Previous 3-mm line survey studies indicated the presence of SiO(2-1) emission towards the clump (Ziurys, Snell & Dickman 1989; van Dishoeck, Jansen & Phillips 1993). In this paper, we present extended maps of the SiO(1-0), SiO(2-1), and $H^{13}CO^+$(1-0) emission towards the molecular clump G. We have used the early results of the SHREC large program to study the mass–energy–momentum injection and density enhancement induced by IC443 on to clump G. With this work, we aim to provide a direct estimate of the impact of SN feedback on the molecular phase of the ISM. The paper is organized as follows. In Section 2, we present the observing method and data acquisition. In Section 3, we present the result of the analysis performed for the SiO and $H^{13}CO^+$ emission towards clump G. Finally, in Sections 4 and 5, we discuss our findings and present our conclusions.

2 OBSERVATIONS

Maps of the SiO(2-1) (86.8469 GHz), $H^{13}CO^+$(1-0) (86.7543 GHz), and $HN^{13}C$(1-0) (87.0909 GHz) emission towards clump G were obtained in 2020 June as part of SHREC (P.I. Giuliana Cosentino). Observations were performed using the 12-m antenna of the ARO (Kitt Peak, Arizona, USA) in on-the-fly (OTF) mode, with scanning speed of $30''$/s and map size of $10' \times 10'$. The map central coordinates are RA $= 06^h16^m32^s$, Dec $= 22^\circ30'45''$. The AROWS receiver was used with tuning frequency of 89.2 GHz and spectral resolution of 78 kHz ($\sim$0.3 km s^{-1} at 86 GHz), providing a bandwidth of 500 MHz.

In 2020 November, we used the 40-m antenna at the Yebes Observatory (Castilla-La Mancha, Spain) to obtain complementary SiO(1-0) (43.4238 GHz) maps (project code 20B009). The SiO(1-0) observations were performed in OTF mode with scanning speed of $15''$/s, central coordinates RA $= 06^h16^m42.4^s$, Dec $= 22^\circ32'26.3''$, and map size $3.5' \times 3.5'$, corresponding to the full extension of the SiO(2-1) emission. We used the Fast Fourier Transform (FFT) spectrometer in *Q* band (tuning frequency of 43.424 GHz), with spectral resolution of 38 kHz ($\sim$0.3 km s^{-1} at 43 GHz) and bandwidth 2.5 GHz.

For both sets of observations, we use the reference position RA $= 06^h19^m01^s$, Dec $= 22^\circ28'11''$. Intensities were measured in units of antenna temperature and converted into main-beam brightness temperatures using beam efficiencies of 0.61 and 0.52, for the ARO and Yebes observations, respectively. The final data cubes were generated using the GILDAS[1] package and have beam sizes of $45''$ and $76''$, for the Yebes and ARO maps, respectively, and a common spectral resolution of 0.5 km s^{-1}. The achieved root-mean-square (rms) per channel and per beam is of 10 mK for the Yebes maps and 30 mK for the ARO maps. We note that the $HN^{13}C$(1-0) emission observed as part of SHREC is found to be below the 3$\times$ rms level across the full map and hence we do not include it in the following analysis.

3 RESULTS

3.1 Morphology and kinematics of the shocked gas

In Fig. 2, we present the three-colour image of the SNR IC443 (left) obtained as part of the WISE all-sky survey (Wright et al. 2010) together with the integrated (in velocity) intensity maps (right) of the SiO(1-0) (top), SiO(2-1) (middle), and $H^{13}CO^+$(1-0) (bottom) emission. The shocked and dense gas emission is coincident with a bright and extended 4.5-μm ridge, a signature of shock-excited gas (Noriega-Crespo et al. 2004), and tracing the SNR shock front. The shocked gas tracer emission shows a morphology that is localized with respect to the 4.5-μm ridge and elongated in the same direction. Such an emission extends $>3\times$ the beam aperture ($\sim$0.4 and $\sim$0.6 pc for Yebes and ARO observations, respectively) and over parsec scales, i.e. $\sim 1.8 \times 1.6$ pc^2. The $H^{13}CO^+$ emission also extends over a parsec scale (1.2×1.3 pc^2) but it appears to be more compact than the SiO emission, i.e. $<2\times$ the beam aperture.

In Fig. 3, we report the moment 1 velocity map (colour scale) obtained for the SiO(1-0), superimposed on the SiO(1-0) integrated intensity emission contours (black). As seen from Fig. 3, the SiO emission shows a velocity gradient, with the blue-shifted gas located towards the east-south-east and the red-shifted emission found towards the west-north-west. Moving away from the 4.5-μm ridge

[1] https://www.iram.fr/IRAMFR/GILDAS

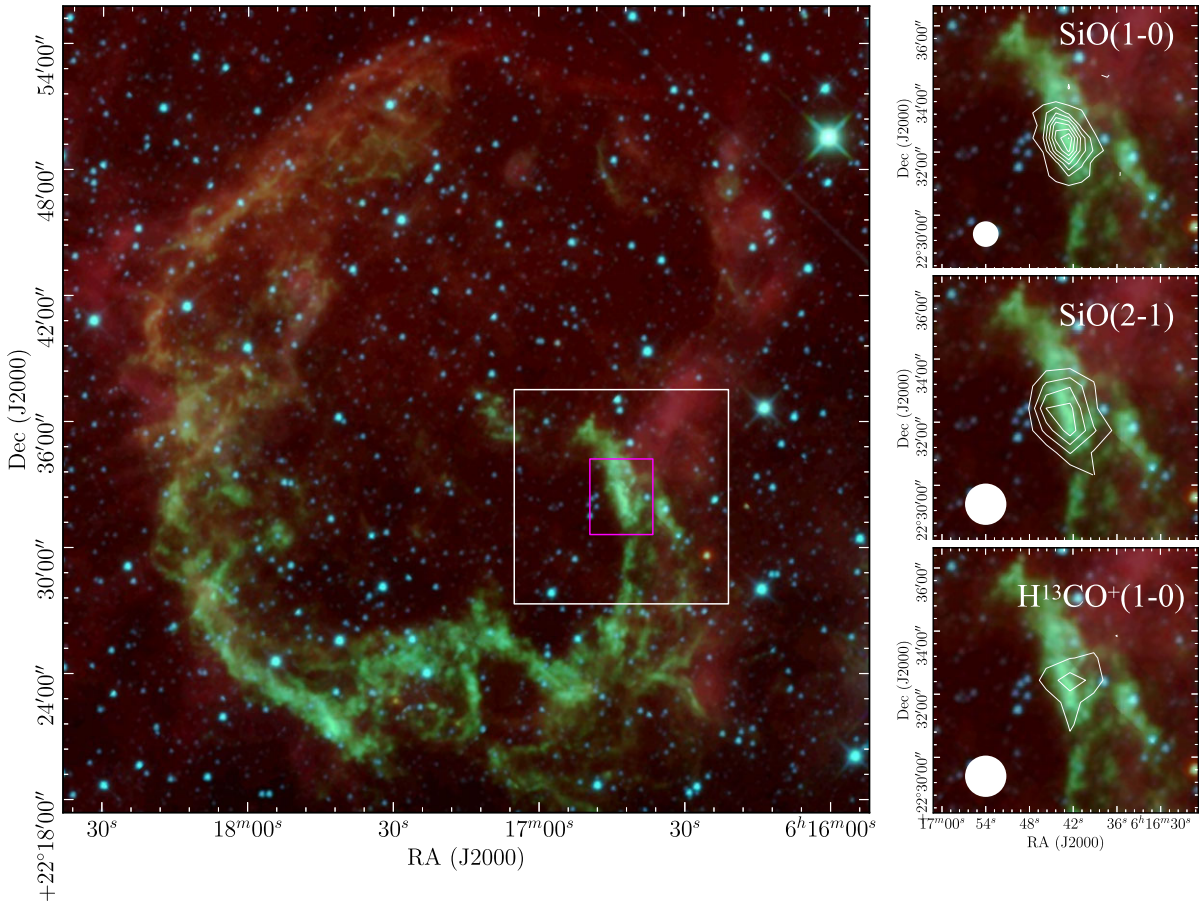

Figure 2. Left: Three-colour image (red = 22 μm; green = 4.6 μm; and blue = 3.4 μm) of the SNR IC443 (WISE all-sky survey Wright et al. 2010). White and magenta rectangles indicate the extent of the ARO and Yebes maps, respectively. Right: Integrated intensity maps (−22; 6 km s^{-1}) of the SiO(1-0) (top; σ = 0.1 K km s^{-1}), SiO(2-1) (middle; σ = 0.2 K km s^{-1}), and H^{13}CO$^+$(1-0) (bottom; σ = 0.2 K km s^{-1}) are shown in white contours (from 3σ in steps of 3σ). The ARO and Yebes beam sizes are shown as white circles in the bottom left of each panel.

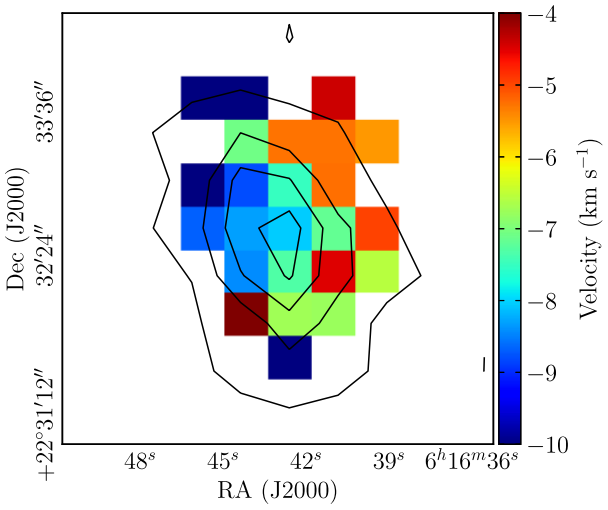

Figure 3. SiO(1-0) moment 1 velocity map (colour scale) towards IC443 superimposed on the SiO(1-0) integrated intensity map contours (black) from 3σ by steps of 6σ (σ = 0.1 K km s^{-1}).

and into the SNR, the SiO velocity is systematically blue-shifted with respect to the central velocity of IC443, i.e. −4.5 km s^{-1}, estimated by means of ^{12}CO and HCO$^+$ observations (White et al. 1987; Dickman et al. 1992; van Dishoeck et al. 1993).

3.2 Excitation conditions of the shocked gas

We now consider the SiO(1-0) and (2-1) line intensities to infer the excitation conditions of the shocked gas, i.e. H_2 number density, n(H_2), SiO column density, N(SiO), excitation temperature, T_{ex}, and how these vary as a function of the gas velocity. For this analysis, the SiO(1-0) emission cube has been spatially smoothed to the same angular resolution of the SiO(2-1) and H^{13}CO$^+$(1-0) maps and all cubes were spectrally smoothed to a velocity resolution of 2 km s^{-1}. The SiO(1-0) (black), SiO(2-1) (red), and H^{13}CO$^+$ (green) spectra obtained by averaging the emission from pixels with signal above 3σ are shown in Fig. 4, along with their respective 3× rms levels (dotted horizontal lines).

From Fig. 4, the SiO(1-0) and SiO(2-1) emission shows significant intensities (>3× rms) for velocity channels in the range of −19.5, −2.5 km s^{-1} (vertical blue dotted–dashed lines). We have therefore limited our analysis to these velocities. For each of the considered velocity channels, we have measured the SiO(1-0) and SiO(2-1) line intensity in unit of K (Table 1) and used the non-Local

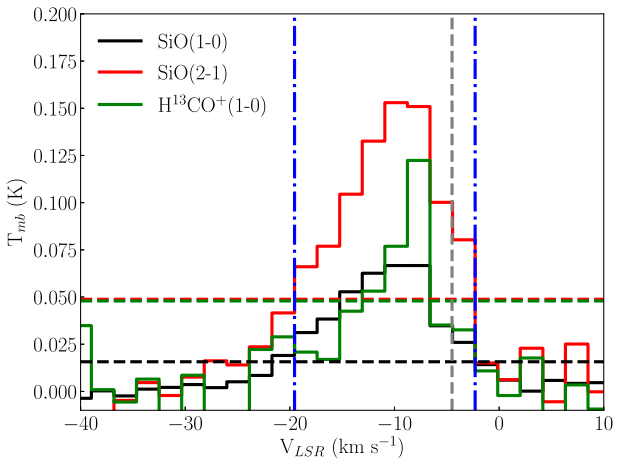

Figure 4. SiO(1-0) (black), SiO(2-1) (red), and $H^{13}CO^+$(1-0) (green) spectra extracted towards the regions of the map with emission above the 3σ levels. The horizontal dashed lines indicate the $3\times$ rms levels for each species. Vertical blue dash–dotted lines indicated the velocity range considered for the comparison with RADEX models. Finally, the vertical grey line indicates the central velocity of IC443.

Thermodynamic Equilibrium (LTE) radiative transfer code RADEX (van der Tak et al. 2007) to estimate the physical conditions that best reproduce the line strength. RADEX uses the large velocity gradient approximation (Sobolev 1957) to predict line intensities of specific molecules in homogeneous interstellar clouds, starting from a pre-defined system geometry and five input parameters. These are the gas kinetic temperature, $T_{\rm kin}$, the temperature of the background material, $T_{\rm bg}$, the volume density of the collisional partners, the molecule column density, N(SiO), and the width of emission line. The RADEX output provides the user with line strengths at several frequencies for the selected molecule as well as excitation temperatures and optical depth estimates for each transition. For our analysis, we have assumed a geometry consistent with that of a slab of material processed by a shock. In addition, we have used H_2 as collisional partner and specified the H_2 volume density, n(H_2), as input parameter. The collisional coefficients between H_2 and SiO were extracted from the LAMDA data base[2] for the first 30 SiO rotational levels (Balança et al. 2018). We have assumed background temperature $T_{\rm bg} = 2.73$ K consistent with the cosmic microwave background emission and used a width of the line of 2 km s^{-1}, corresponding to the velocity width of each channel. Since only two SiO rotational transitions are here observed, it is not possible to constrain at the same time the three remaining parameters, n(H_2), N(SiO), and $T_{\rm kin}$. Therefore, in the following analysis, we proceed by assuming a certain value of $T_{\rm kin}$ and investigate the sensitivity of our results with respect to this assumption. In Fig. 5, we show multiple grids of RADEX models obtained for n(H_2) in the range of 10^2–10^9 cm^{-3}, N(SiO) in the range of 10^9–10^{16} cm^{-2}, and with fixed $T_{\rm kin}$ of 10 K, 20 K, 50 K, and 100 K.

As shown in Fig. 5, the excitation temperature of the SiO(1-0) transition varies significantly for different values of kinetic temperature. In particular, already at $T_{\rm kin}>20$ K, RADEX predicts negative excitation temperatures for the SiO(1-0) emission, i.e. the SiO(1-0) emission is predicted to behave as a maser. SiO(1-0) maser emission is commonly detected towards different objects, e.g. variable stars (Cho, Lee & Park 2007), massive young stellar objects (YSOs) (Issaoun et al. 2017), and massive star clusters (Verheyen, Messineo & Menten 2012), but the rotational transition is usually observed to also be vibrationally excited. At the best of our knowledge, the vibrational ground state of SiO $J = 1$-0 here analysed has been observed with characteristics typical of maser emission only towards evolved stars (Boboltz & Claussen 2004). Towards these objects, the transition shows brightness temperatures of $>10^3$ K, much higher that the intensities observed here, and is usually detected simultaneously to higher vibrational transitions at close frequencies (∼43.1 GHz). Such frequencies are covered by the bandwidth of our Yebes observations but no vibrationally excited emission is detected. We therefore conclude that the SiO(1-0) emission here reported does not show characteristics typical of maser emission and assume $T_{\rm kin} = 15$ K in the following analysis. Our assumption of $T_{\rm kin} < 20$ K reproduces well the observed excitation of the SiO line emission and excludes the possibility that $T_{\rm ex} < 0$ K (maser effects). We also note that the assumed $T_{\rm kin}$ is consistent with that estimated for the shocked CO emission by Dell'Ova et al. (2020) and only a factor of 2 lower than that reported by Ziurys et al. (1989), using multiple Ammonia (NH_3) transitions ($T_{\rm kin} \sim 33$ K).

Our final grid consists of 250 000 models with n(H_2) in the range of $\sim 10^2$–10^7 cm^{-3} and N(SiO) in the range of $\sim 10^9$–10^{16} cm^{-2}, $T_{\rm kin} = 15$ K, $T_{\rm bg} = 2.73$ K, and line width = 2 km s^{-1}. The Si(1-0) line intensities, $I_{(1-0)}$ (left-hand panel), and the SiO(2-1)/SiO(1-0) line intensity ratios, $I_{(2-1)}/I_{(1-0)}$ (right-hand panel), predicted by our grid of models are shown in Fig. 6.

For each of the considered velocity channels, we have compared the measured SiO(1-0) and (2-1) intensities with those predicted by all models in the grid and computed the associated chi square, χ^2, according to the following:

$$\chi^2 = \left[\frac{(I_{1-0} - I_{\rm RAD})^2}{(\Delta I_{1-0})^2} + \frac{(I_{2-1} - I_{\rm RAD})^2}{(\Delta I_{2-1})^2} \right], \quad (1)$$

where I_{1-0} and I_{2-1} are the observed intensities of the SiO(1-0) and (2-1) lines and the subscripts RAD indicate the corresponding quantities estimated by RADEX. For each pair of intensity values, the uncertainty is estimated as the rms per channel, i.e. 5 mK and 15 mK for SiO(1-0) and SiO(2-1), respectively.

For each velocity channel, we have extracted a best model as the one that minimizes the χ^2 and a range of best RADEX models as those for which $\chi^2 < 1$. The obtained best values and ranges are reported in Table 1, along with the central velocity of the channel and the measured SiO intensities. Since only one transition has been observed for $H^{13}CO^+$, a similar analysis is not possible for this dense gas tracer. Hence, we have assumed $H^{13}CO^+$(1-0) to have excitation temperatures similar to that estimated for SiO(2-1) and used the best RADEX values at each velocity step to estimate the $H^{13}CO^+$ column density. This is justified by the fact that the SiO(2-1) and $H^{13}CO^+$(1-0) transitions have a similar critical density. The obtained values are reported in column 9 of Table 1.

In Fig. 7, the best values (dot markers) and acceptable ranges (vertical lines) obtained for the n(H_2) (right-hand panel), N(SiO) (middle panel), and $T_{\rm ex}$ (left-hand panel) are shown along with the SiO(1-0) (black) and SiO(2-1) (red) spectra. From Fig. 7, the n(H_2) decreases from red- to blue-shifted velocities. For $V_{\rm LSR} > -5$ km s^{-1}, the volume density is $>5 \times 10^5$ cm^{-3}, while for $V < -5$ km s^{-1}, the volume density decreases and sets on a relatively constant value ($\sim 1.5 \times 10^5$ cm^{-3}). A similar trend is observed for the SiO excitation temperatures (right-hand panel), where the two distributions hint to a higher excitation of the gas at red-shifted velocities, i.e. where the $T_{\rm ex}^{2-1}$ increases and the $T_{\rm ex}^{1-0}$ decreases.

[2] https://home.strw.leidenuniv.nl/ moldata/SiO.html

Table 1. Results of the RADEX analysis performed for the SiO and $H^{13}CO^+$ emission. For each velocity channel, the central velocity; the SiO(1-0), SiO(2-1), and $H^{13}CO^+$(1-0) intensities; the best n(H_2), N(SiO), and T_{ex} values; and ranges are reported. We note that all the measured $H^{13}CO^+$ intensities are at least higher than 1× the corresponding rms of 15 mK.

V (km s^{-1})	I_{1-0} (K)	I_{2-1} (K)	n(H_2) ($\times10^5$ cm^{-3})	N(SiO) ($\times10^{11}$ cm^{-2})	T_{ex}^{1-0} (K)	T_{ex}^{2-1} (K)	$I_{H^{13}CO^+}$ (K)	N($H^{13}CO^+$) ($\times10^{10}$ cm^{-2})
−18.5	0.031	0.066	1.7 (0.8–4.8)	2.6 (2.2–3.0)	26 (20–26)	8 (6–13)	0.020	3.5
−16.5	0.038	0.077	1.4 (0.8–3.0)	3.0 (2.8–3.5)	25 (19–26)	8 (6–11)	0.017	3.0
−14.5	0.053	0.104	1.4 (0.9–2.3)	4.2 (3.9–4.6)	25 (21–26)	8 (6–10)	0.043	7.0
−12.5	0.063	0.133	1.7 (1.2–2.6)	5.3 (4.9–5.6)	25 (23–25)	8 (7–10)	0.053	9.5
−9.5	0.067	0.153	2.0 (1.5–3.2)	5.8 (5.4–6.4)	25 (23–25)	9 (8–11)	0.077	13
−7.5	0.067	0.151	2.0 (1.4–3.1)	5.8 (5.4–6.2)	25 (23–25)	9 (8–11)	0.122	22
−5.5	0.035	0.100	5.9 (2.1–100)	3.9 (3.2–5.8)	20 (15–25)	13 (9–15)	0.035	6.5
−3.5	0.026	0.080	13.8 (2.2–100)	3.5 (2.4–4.6)	17 (15–25)	15 (9–15)	0.033	6.3

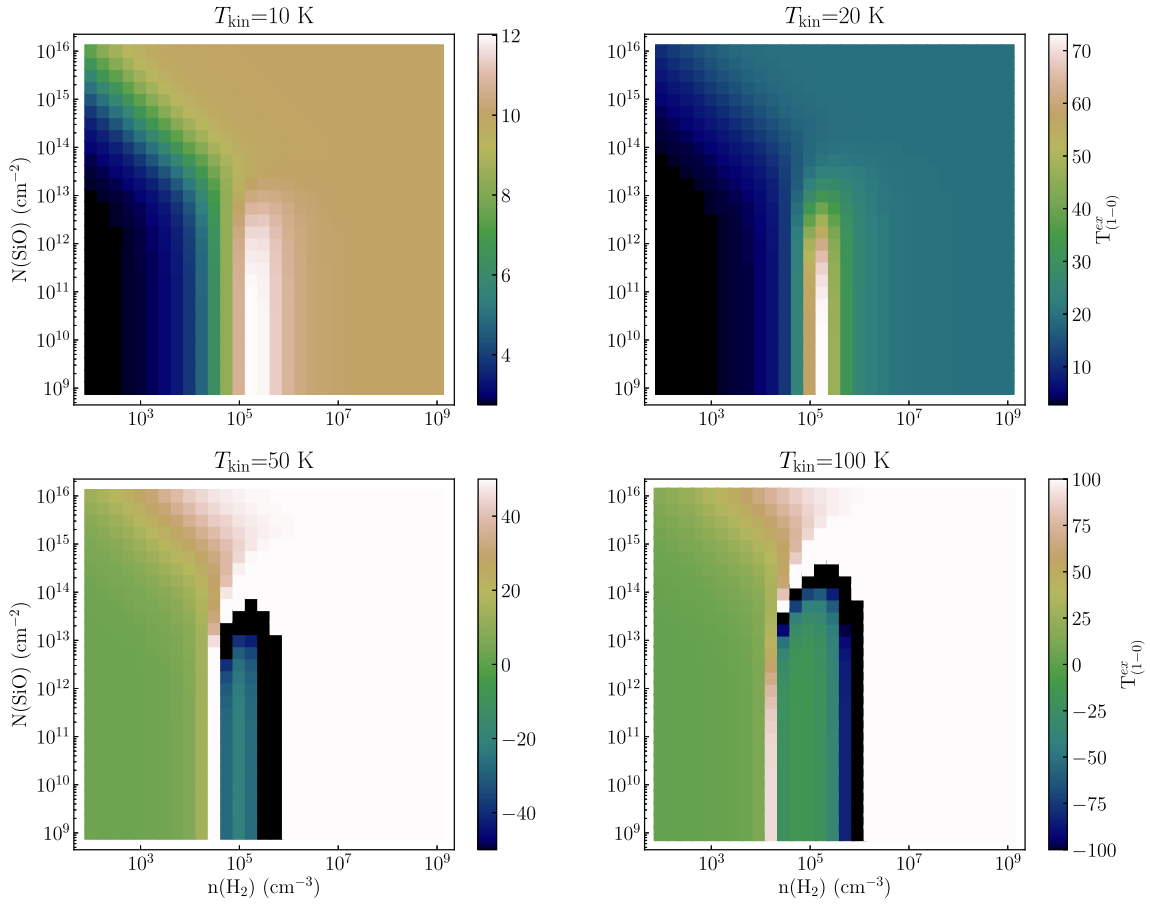

Figure 5. Grids of RADEX models obtained for n(H_2) in the range of 10^2–10^9 cm^{-3}, N(SiO) in the range of 10^9–10^{16} cm^{-2}, and T_{kin} of 10 K (top left), 20 K (top right), 50 K (bottom left), and 100 K (bottom right). For each set of N(H_2), N(SiO), and T_{kin}, the T_{ex} predicted for the SiO(1-0) transition is shown in colour scales. Although here not shown for simplicity, the T_{ex} of the SiO(2-1) transitions shows similar trends as a function of kinetic temperature.

From the right-hand panel in Fig. 7, the T_{ex} estimated for the SiO(1-0) transition is >15 K at all velocities, i.e, higher than the kinetic temperatures assumed in our models. This *supra-thermal* excitation is a known behaviour, typically observed for linear molecules and at densities consistent with the critical density ($n_{crit} \sim 4 \times 10^4$ cm^{-3} for the $J = 1$-0 SiO transition). Depending on the H_2 and SiO number densities, the radiative and collisional excitation of the SiO compete and LTE conditions are expected to be achieved when collisional excitation dominates. Hence, the T_{ex} is expected to be at most equal to T_{kin}. However, due to quantum selection rules, radiative transitions in linear molecules occur only between successive rotational levels ($\Delta J = \pm1$). Furthermore, the Einstein coefficient A, describing spontaneous radiative decay, increases with the J of the transition. As a consequence of these two effects, higher J levels will be de-excited faster than the low J levels, causing a supra-population of the low-J states, and resulting in T_{ex} rising above the LTE value. Such

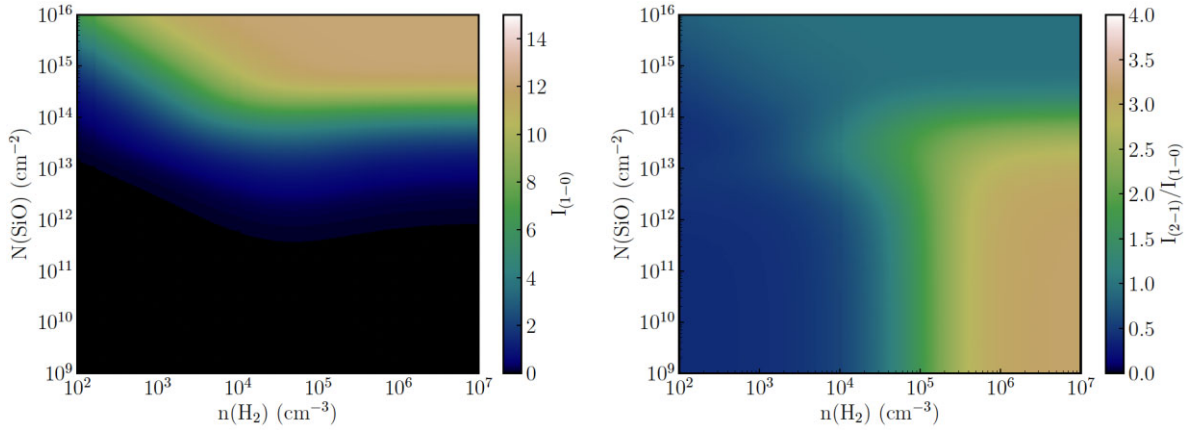

Figure 6. SiO(1-0) line intensities, $I_{(1-0)}$ (left), and SiO(2-1)/SiO(1-0) line intensity ratios, $I_{(2-1)}/I_{(1-0)}$ (right), as predicted by the final grid of model obtained for $T_{\rm kin}$ = 15 K.

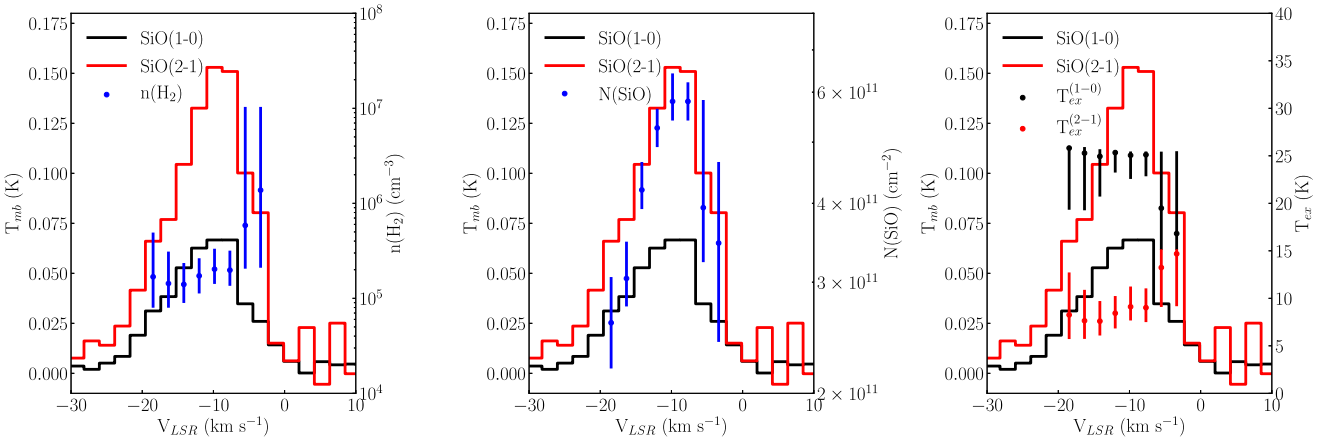

Figure 7. SiO(1-0) (black) and SiO(2-1) (red) spectra as shown in Fig. 2 and with superimposed the best values (dot markers) and ranges (vertical lines) obtained for n(H$_2$) (blue, left-hand panel), N(SiO) (blue, middle panel), and the two excitation temperatures $T_{\rm ex}^{1-0}$ (black, right-hand panel) and $T_{\rm ex}^{2-1}$ (red, right-hand panel).

behaviour is analysed in details by Koeppen & Kegel (1980) for the CO molecule.

3.3 Energy, mass, and momentum

As last step in our analysis, we have estimated the mass (M), momentum (P), and kinetic energy (E) of the SiO and H^{13}CO$^+$ emission, using the method described in Dierickx et al. (2015):

$$M = \frac{d^2}{\chi(\rm mol)} \times \mu_{\rm g} m({\rm H_2}) \times \Sigma_{\rm pix} N({\rm mol})_{\rm pix}, \quad (2)$$

$$P = MV, \quad (3)$$

$$E = \frac{1}{2} MV^2, \quad (4)$$

where d is the source kinematic distance (1.9 kpc; Ambrocio-Cruz et al. 2017), $\mu_{\rm g}$ = 1.36 is the gas molecular weight, m(H$_2$) is the molecular hydrogen mass, χ(mol) is the fractional abundance with respect to H$_2$, and $\Sigma_{\rm pix}$N(mol)$_{\rm pix}$ is the total column density of the molecule, summed for all pixels with signal above 3σ. Finally, V is the line width at the base (3× rms) of the emission. Similar to what described in Cosentino et al. (2018), we have obtained an estimate of the χ(SiO) by considering the following equation:

$$\chi({\rm SiO}) = \frac{\rm N(SiO)}{\rm N(H^{13}CO^+)} \times \chi({\rm HCO^+}) \times \frac{^{13}C}{^{12}C}, \quad (5)$$

where N(SiO) ∼ (3.3 ± 0.5) × 10^{12} cm^{-2} and N(H^{13}CO$^+$) ∼(7 ± 1) × 10^{11} cm^{-2} have been obtained by summing the values reported in Table 1. The corresponding uncertainties have been obtained by considering the N(SiO) variability ranges in Table 1 and by assuming that both the SiO and H^{13}CO$^+$ column densities have the same relative error. Hence, we have assumed ^{12}C/^{13}C ∼ 50 ± 10, i.e. we have assigned a 20 per cent uncertainty (e.g. Zeng et al. 2017). We note that the assumed ^{12}C/^{13}C value is consistent with that reported by Dell'Ova et al. (2020), towards clump G. Finally, we assume χ(HCO$^+$) ∼ (1 ± 0.5) × 10^{-8}, as reported by van Dishoeck et al. (1993). We thus estimated the SiO and H^{13}CO$^+$ abundances with respect to H$_2$ to be χ(SiO) ∼ (1 ± 0.5) × 10^{-9} and χ(H^{13}CO$^+$) ∼ (2 ± 1) × 10^{-10}.

In order to estimate the SiO and H^{13}CO$^+$ column densities at each pixel, we have assumed $T_{\rm ex}$ ∼ 10 K for both species, obtained as the average of the values reported in Table 1 for SiO(2-1). Hence, we use the H^{13}CO$^+$(1-0) and SiO(2-1) transitions to estimate the energy, mass, and momentum of the dense and shocked gas, respectively. As reported in Table 2, we obtain M ∼ 125 ± 50 and 100 ± 60 M$_\odot$,

Table 2. Mass (M), momentum (P), and energy (E) obtained for the shocked and dense gas and corresponding velocity ranges used for the calculation.

Molecule	M ($M_\odot$)	P ($M_\odot$ km s^{-1})	E (erg)	ΔV (km s^{-1})
$H^{13}CO^+$	125 ± 50	$(8 \pm 3) \times 10^2$	$(4.5 \pm 1.8) \times 10^{40}$	6
SiO	100 ± 60	$(2 \pm 1) \times 10^3$	$(2.6 \pm 1.6) \times 10^{41}$	16

$P \sim (8 \pm 3) \times 10^2$, and $P \sim (2 \pm 1) \times 10^3$ $M_\odot$ km s^{-1}, and $E \sim (4.5 \pm 1.8) \times 10^{40}$ and $\sim (2.6 \pm 1.6) \times 10^{41}$ ergs for $H^{13}CO^+$ and SiO, respectively. The uncertainties have been obtained by following the standard propagation rules.

4 DISCUSSION

4.1 Can the SiO emission be due to molecular outflows powered by embedded protostars?

The shock interaction between IC443 and clump G has been largely investigated from both an observational (e.g. Ziurys et al. 1989; Dickman et al. 1992; van Dishoeck et al. 1993; Reach et al. 2019; Dell'Ova et al. 2020; Kokusho et al. 2020) and theoretical (e.g. Troja et al. 2006, 2008; Ustamujic et al. 2021) point of view. However, SiO is usually widely observed in regions of ongoing star formation activity (e.g. Codella et al. 2007; López-Sepulcre et al. 2011; Liu et al. 2020). Hence, we now discuss the possibility that the SiO emission observed towards clump G may be due to molecular outflows driven by deeply embedded protostars.

As reported in Table 2, the energy measured for the shocked gas is $\sim 2.6 \times 10^{41}$ ergs. This is several orders of magnitudes lower than the typical kinetic energy measured for molecular outflows powered by high-mass protostars, i.e. $\sim 10^{46}$ ergs (e.g. Zhang et al. 2005; López-Sepulcre et al. 2009), and intermediate-mass protostars, i.e. $\sim 10^{43}$–10^{44} ergs (e.g. Beltrán, Girart & Estalella 2006; Beltrán et al. 2008). We therefore exclude the possibility that ongoing high-mass and intermediate-mass star formation may be driving the observed SiO emission. On the other hand, Dell'Ova et al. (2020) reported the presence of $\sim$25 YSOs spatially associated with the shocked gas in clump G and located within a distance of $\pm$500 pc (see fig. 14 in Dell'Ova et al. 2020). We now assume that the SiO emission is entirely due to putative outflows powered by these 25 YSOs, and that each source contributes equally to the final SiO emission. In this scenario, each outflow should have on average a mass of $M_{SiO}/25 \sim 4$ $M_\odot$ and a momentum of $P_{SiO}/25 \sim 80$ $M_\odot$ km s^{-1}. These estimates are several orders of magnitude higher than those typically measured towards molecular outflows driven by low-mass protostars, i.e. $M \sim 0.005$–0.15 $M_\odot$, $P \sim 0.004$–0.12 $M_\odot$ km s^{-1} (e.g. Dunham et al. 2014). This is even more stringent if we consider the more likely scenario in which only few of the 25 YSOs are effectively driving outflows and thus contributing to the observed SiO emission. Hence, although we cannot exclude that a small contribution to the observed SiO emission may be due to molecular outflows powered by low-mass protostars, the major contribution to the observed SiO emission likely arises from the large-scale shock interaction occurring between IC443 and clump G.

4.2 SiO as probe of the shock interaction between IC443 and clump G: positive feedback driven by SNRs

The presence of such a large-scale shock interaction is further supported by the kinematic structure observed for the SiO emission and reported in Section 3.1. The SiO emission is indeed significantly blue-shifted with respect to the central velocity of the clump (Dickman et al. 1992) and it presents a global velocity gradient with the blue-shifted emission appearing towards the east-south-east and the red-shifted gas located towards the west-north-west. Such a kinematic structure cannot be reproduced by a collection of molecular outflows driven by low-mass protostars, which have been seen to be randomly oriented with respect to the parental clump, in star-forming regions (Dunham et al. 2016; Stephens et al. 2017). On the contrary, the well-organized SiO kinematic structure is similar to that reported by Cosentino et al. (2019) towards the molecular cloud G034 known to be interacting with the SNR W44 (Wootten 1977). Towards this region, the SiO emission is seen to be blue-shifted with respect to the central velocity of the cloud (42 km s^{-1} Cosentino et al. 2019) and spatially associated with a 4.5-μm extended ridge (Cosentino et al. 2018). The SiO emission towards G034, as seen with ALMA, shows a sharp gradient of 2–3 km s^{-1}, within 3″, which is followed by a shallower gradient of 5–6 km s^{-1}, across >10″ scales (equivalent to linear scales of 0.15 pc). Our ARO and Yebes observations probe spatial scales of 0.7–0.4 pc and therefore cannot resolve with such detail the observed SiO emission. However, IC443 is 1 kpc closer than W44 ($\sim$2.9 kpc) and its SiO emission is almost a factor of 2 more extended, which allows us to appreciate a clear shocked gas velocity gradient across the ridge. The highly blue-shifted SiO gas here observed is naturally explained when the geometry suggested by Troja et al. (2006) is considered. In this scenario, clump G is located in the foreground with respect to IC443 and hence the shock wave released by the SNR hits the clump from behind pushing and dragging the shocked gas towards the observer. The fact that the SiO blue-shifted emission appears directed towards the inner part of IC443 is likely due to the fact that the shock is impacting on the cloud with a certain angle with respect to the line of sight. This was first suggested by Dickman et al. (1992) and van Dishoeck et al. (1993) and is consistent with what was reported by Reach et al. (2019). These authors modelled the interaction between IC443 and clump G as occurring through two CJ-type shocks of $\sim$60 km s^{-1}and $\sim$37 km s^{-1} and dynamical age 5×10^3 and 3×10^3 yr, respectively, and that are hitting the cloud with angles of $\sim$60–65° with respect to the line of sight.

The multiple shocks driven by IC443 and impacting on clump G may be responsible for the H_2 volume density profile reported in Fig. 7. The higher densities seen at velocity ≥ -5 km s^{-1} may be associated with the initial stronger impact between the shocks and the cloud, from which the bulk of the SiO emission is likely arising. After this first compression, the gas is dragged and decelerates towards the observer, appearing as highly blue-shifted. This is also supported by the fact that the higher excitation of the shocked gas also occurs at velocity ≥ -5 km s^{-1} and decreases at more blue-shifted velocities.

From Fig. 7, the H_2 volume density of the shocked gas towards clump G is $\geq 10^5$ cm^{-3} at all velocities, consistent with both the SiO(1-0) and (2-1) critical densities. These values are comparable to those required to ignite star formation in the ISM (e.g. Parmentier 2011).

Towards clump G, several studies have reported H_2 volume densities of the pre-shocked gas in the range $n(H_2) \sim 10^3$–10^4 cm^{-3} (van Dishoeck et al. 1993; Dell'Ova et al. 2020), i.e. slightly lower than those typically observed in dark clouds. This suggests that the shock propagation enhances the gas density by more than a factor of 10 and up to a factor of 100. By using *XMM–Newton* observations of clump G, Troja et al. (2006) identified a strong X-ray absorption and reported an n(H) column density variation, along the line of sight, of 5×10^{21} cm^{-2}. By considering such a

variation and the post-shocked H_2 gas density here measured, i.e. 10^5 cm^{-3}, the length of the shocked region can be estimated as $\sim 2.5 \times 10^{16}$ cm (or 0.008 pc). When a shock velocity of 25 km s^{-1} is considered (Dickman et al. 1992), the time since the first shock interaction is therefore of ∼300 yr. For such a time-scale, a factor of 10 density enhancement in the post-shocked gas can be explained as due to both the shock propagation, the presence of radiative cooling processes, and significant energy dissipation by particles acceleration. The presence of such mechanisms is indicated by the detection of non-thermal X-ray emission, towards clump G (e.g. Bocchino & Bykov 2000). A factor of 100 is instead well beyond the typical density enhancements caused by shock propagation. We therefore suggest that the pre-shocked gas density towards clump G is at least of n(H_2) $\sim 10^4$ cm^{-3}. This supports the idea that clump G may have been a coherent dense structure pre-existent to the SNe event.

Finally, we note that the high density measured in the post-shocked gas may help to explain the enhanced γ-ray emission measured towards clump G (Albert et al. 2007; Acciari et al. 2009; Abdo et al. 2010).

4.3 The $H^{13}CO^+$(1-0) emission towards clump G: shock chemistry product or molecular cloud in the making?

Emission from $H^{13}CO^+$ is a good probe of the dense gas distribution in molecular clouds (e.g. Vasyunina et al. 2011). As shown in Fig. 2, the $H^{13}CO^+$ emission is spatially coincident with the shocked gas emission but less extended. No significant $H^{13}CO^+$ emission is detected outside the shocked region, supporting the low-density values measured for the ambient gas (van Dishoeck et al. 1993). In addition, the $H^{13}CO^+$ spectrum reported in Fig. 4 shows a profile similar to that of both the SiO(1-0) and (2-1) transitions. The spatial and spectral similarities between the SiO and $H^{13}CO^+$ emission hint towards a common nature of the two species. In this scenario, the $H^{13}CO^+$ emission is likely a consequence of the ongoing shock chemistry. Indeed, emission from ions such as HCO^+ is known to be enhanced either in the earliest stages of the shock (see fig. 5 in Flower & Pineau des Forêts 2003) or in the far post-shock gas, when the temperatures have gone down to ∼30 K (Bergin, Snell & Goldsmith 1996). This scenario is consistent with the idea that the cloud was preexistent with respect to the SNR, as already suggested by Dickman et al. (1992), more recently discussed by Ustamujic et al. (2021) and as discussed in Section 4.2. This is also supported by the fact that the dense and shocked gas mass estimates are similar and that the emission is spatially localized with respect to the 4.5-μm ridge, direct probe of the shock front.

Alternatively to this scenario, the $H^{13}CO^+$ emission may be probing the material of clump G that is being shock-compressed with a process similar to that described by Inutsuka et al. (2015). Here, bubbles due to stellar feedback expand into the clumpy multiphase ISM, driving multiple episodes of shock compression into the nearby low-density material participating in the assembling of dark clouds. In the IC443 scenario, preexistent low-density material of clump G may have been compressed by the propagating shocks to densities sufficient to enable the collisional excitation of the $H^{13}CO^+$(1-0). This may be supported by the fact that the dense gas mass reported in Table 2 is comparable to the mass of the ambient gas measured from multiple CO transitions by Dell'Ova et al. (2020). However, we note that the peak velocity of the $H^{13}CO^+$ emission (∼−8 km s^{-1}) does not coincide with that of the ambient cloud in Dell'Ova et al. (2020) (∼−3.5 km s^{-1}). We therefore suggest that the $H^{13}CO^+$ emission is mainly due to the ongoing shock chemistry in IC443. We note that the dense gas mass here estimated from $H^{13}CO^+$ is a factor of 2–3 higher than that reported by Dickman et al. (1992) for clump G, i.e. ∼40 $M_\odot$, obtained from HCO^+ emission. However, these authors did not take into account possible optical depth effects in the HCO^+ emission.

4.4 Negative feedback driven by IC443: comparing observations with model predictions.

In Section 3.3, we have investigated the mass, energy, and momentum calculated for both the dense and shocked gas detected towards clump G. As reported in Table 2, we estimate a mass of the shocked gas of $\sim 100 \pm 60$ $M_\odot$. Considering the length of the shocked region reported in Section 4.2, i.e. 2.5×10^{16} cm or 0.008 pc, the volume of the shocked region is $1.8 \times 1.6 \times 0.008$ pc^3. For the measured post-shocked gas density of n(H_2) $\sim 10^5$ cm^{-3}, the mass enclosed in such a volume is ∼90 $M_\odot$. This provides an independent confirmation to the values reported here.

IC443 is known to be interacting with the molecular material towards three additional sites, named clumps A, B, and C (Dickman et al. 1992). Assuming that the momentum transferred into clumps A, B, and C is equal to that measured towards clump G, we estimate a momentum transferred from the SNR into the surrounding *molecular* material in the range of ~ 3.2–8×10^3 $M_\odot$ km s^{-1}. Since the strongest interaction is known to be occurring towards clump G (Claussen et al. 1997), such a value should be regarded as an upper limit.

State-of-the-art numerical simulations predict the amount of momentum transferred from an expanding SNR into the nearby ISM to be $(1\text{-}5) \times 10^5$ $M_\odot$ km s^{-1}, when a kinetic energy of 10^{51} ergs released by the SNR is assumed (Iffrig & Hennebelle 2015; Kim & Ostriker 2015; Li et al. 2015; Martizzi et al. 2015; Zhang & Chevalier 2019). Assuming such kinetic energy for IC443 (Ustamujic et al. 2021), we estimate that the momentum carried away by the interaction between the SNR shocks and the surrounding molecular material represents <10 per cent of the total imprinted momentum.

More in general, considering the momentum of the shocked and dense gas reported in Table 2, 2×10^3 $M_\odot$ km s^{-1}, and the SiO and $H^{13}CO^+$ emission spatial coverage of 1.8×1.6 pc^2 and 1.3×1.2 pc^2, respectively, we estimate the *momentum per unit area* of the gas to be ∼500–690 $M_\odot$ km s^{-1}pc^2. For this estimate, we assume the gas emission to be plane-parallel and along the line of sight. We note that the momentum per unit area here estimated should also be regarded as an upper limit, since the interaction towards other sites is likely to be weaker than that observed towards clump G. Considering for the SNR a diameter of 45″ (Green 2019), we estimate the area of the bubble to be ∼1800 pc^2. Since the molecular material surrounding IC443 is distributed as a toroid around the expanding bubble (Troja et al. 2006), we assume that the SNR effective area that is directly in contact with molecular material is ∼20 per cent and in any case <50 per cent, since IC443 is expanding into an atomic cloud in the North. Therefore, we estimate the momentum carried by the molecular material to be ~ 1.8–2.5×10^5 $M_\odot$ km s^{-1}. This is 35–50 per cent the momentum typically injected by an SNR.

Our calculation indicates that the molecular material can be a relevant carrier of the momentum injected by SNR feedback into the ISM. The importance of this resides in the fact that the cold dense molecular material of the ISM is the primary fuel of star formation in galaxies. The imprinted momentum contributes to maintain the level of turbulence in the ISM (Padoan et al. 2016), a key ingredient in the star formation process. Finally, we note that the momentum deposited by SNRs into the ISM is further increased by the presence

of accelerated cosmic rays. Since their energy is not radiated away during the Sedov–Taylor phase, cosmic ray further supports the SNR expansion and prolongs the momentum deposition phase. As a result, the momentum injected by SNRs into the nearby material can be boosted by a factor of 5–10 for density of the ISM $>10^2$ cm^{-3}. For a more detailed discussion, we refer to Diesing & Caprioli (2018).

5 CONCLUSIONS

In this paper, we have used SiO(2-1) and $H^{13}CO^+$(1-0) observations obtained as part of SHREC as well as complementary SiO(1-0) observations obtained by 40-m antenna at the Yebes Observatory to investigate the negative and positive feedback driven by the SNR IC443 on to the molecular clump G. Our results can be summarized as follows:

(i) The SiO emission shows an elongated morphology, spatially coincident and parallel to an extended ridge of shocked gas seen at 4.5 μm. The SiO kinematics is organized as a well-ordered structure, with the shocked material being systematically blue-shifted with respect to the central velocity of the SNR.

(ii) The shocked gas kinematic structure as well as its inferred mass (100 $M_\odot$), momentum (2×10^3 $M_\odot$ km s^{-1}), and energy (2.6×10^{41} ergs) cannot be solely explained as the product of ongoing star formation activity in clump G. Therefore, we conclude that the bulk of the SiO emission arises from the ongoing shock interaction between the clump and IC443.

(iii) Towards clump G, the shock propagation enhances the gas density to values $n(H_2) \geq 10^5$ cm^{-3}, a factor of >10 higher than the density of the pre-shocked material and consistent with the densities required to ignite star formation in molecular clouds.

(iv) The dense gas mass estimated from the $H^{13}CO^+$ emission is similar to that estimated for the shocked gas. Furthermore, the dense gas emission is spatially concentrated towards the 4.5-μm ridge. We interpret this result as evidence that the $H^{13}CO^+$ emission is likely due to shock chemistry effects and that clump G was preexistent with respect to IC443.

(v) Finally, we estimate that between 35 per cent and 50 per cent of the momentum injected by IC443 is transferred to the molecular phase of the ISM, making the molecular material an important momentum carrier in sites of SNR–cloud interactions. The injected momentum helps to maintain turbulence in the molecular ISM that fuels star formation in galaxies.

ACKNOWLEDGEMENTS

We thank Prof. Floris van der Tak for providing us with helpful insights on the matter of the SiO supra-thermal excitation. GC and PG acknowledge support from a Chalmers Cosmic Origins postdoctoral fellowship. IJ-S has received partial support from the Spanish State Research Agency (AEI; project number PID2019-105552RB-C41). RF acknowledges funding from the European Union's Horizon 2020 research and innovation programme under the Marie Sklodowska-Curie grant agreement no. 101032092. JCT acknowledges support from ERC project 788829- MSTAR. S.V. acknowledges partial funding from the European Research Council (ERC) advanced grant MOPPEX 833460. SZ acknowledges support from NAOJ ALMA Scientific Research grant number 2016-03B.

DATA AVAILABILITY

The SiO and $H^{13}CO^+$ data cubes used for the study here presented will be distributed upon request to the corresponding author. Data obtained as part of SHREC will also be made publicly available through dedicated website in the coming months.

REFERENCES

Abdo A. A. et al., 2010, ApJ, 712, 459
Acciari V. A. et al., 2009, ApJ, 698, L133
Agertz O., Teyssier R., Moore B., 2011, MNRAS, 410, 1391
Agertz O., Kravtsov A. V., Leitner S. N., Gnedin N. Y., 2013, ApJ, 770, 25
Albert J. et al., 2007, ApJ, 664, L87
Ambrocio-Cruz P., Rosado M., de la Fuente E., Silva R., Blanco-Piñon A., 2017, MNRAS, 472, 51
Balança C., Dayou F., Faure A., Wiesenfeld L., Feautrier N., 2018, MNRAS, 479, 2692
Bally J., 2011, in Alves J., Elmegreen B. G., Girart J. M., Trimble V., eds, Proc. IAU Symp. 270, Computational Star Formation. p. 247
Beltrán M. T., Girart J. M., Estalella R., 2006, A&A, 457, 865
Beltrán M. T., Estalella R., Girart J. M., Ho P. T. P., Anglada G., 2008, A&A, 481, 93
Bergin E. A., Snell R. L., Goldsmith P. F., 1996, ApJ, 460, 343
Bigiel F., Leroy A., Walter F., Brinks E., de Blok W. J. G., Madore B., Thornley M. D., 2008, AJ, 136, 2846
Bigiel F., Leroy A., Walter F., Blitz L., Brinks E., de Blok W. J. G., Madore B., 2010, AJ, 140, 1194
Blondin J. M., Wright E. B., Borkowski K. J., Reynolds S. P., 1998, ApJ, 500, 342
Boboltz D. A., Claussen M. J., 2004, ApJ, 608, 480
Bocchino F., Bykov A. M., 2000, A&A, 362, L29
Caselli P., Hartquist T. W., Havnes O., 1997, A&A, 322, 296
Ceverino D., Klypin A., 2009, ApJ, 695, 292
Chevalier R. A., 1974, ApJ, 188, 501
Chevalier R. A., 1999, ApJ, 511, 798
Cho S.-H., Lee C. W., Park Y.-S., 2007, ApJ, 657, 482
Cioffi D. F., McKee C. F., Bertschinger E., 1988, ApJ, 334, 252
Claussen M. J., Frail D. A., Goss W. M., Gaume R. A., 1997, ApJ, 489, 143
Codella C., Cabrit S., Gueth F., Cesaroni R., Bacciotti F., Lefloch B., McCaughrean M. J., 2007, A&A, 462, L53
Cornett R. H., Chin G., Knapp G. R., 1977, A&A, 54, 889
Cosentino G. et al., 2018, MNRAS, 474, 3760
Cosentino G. et al., 2019, ApJ, 881, L42
Dalla Vecchia C., Schaye J., 2012, MNRAS, 426, 140
Dell'Ova P. et al., 2020, A&A, 644, A64
Denoyer L. K., 1979, ApJ, 232, L165
Dickman R. L., Snell R. L., Ziurys L. M., Huang Y.-L., 1992, ApJ, 400, 203
Dierickx M., Jiménez-Serra I., Rivilla V. M., Zhang Q., 2015, ApJ, 803, 89
Diesing R., Caprioli D., 2018, Phys. Rev. Lett., 121, 091101
Dubois Y., Teyssier R., 2008, A&A, 477, 79
Dumas G., Vaupré S., Ceccarelli C., Hily-Blant P., Dubus G., Montmerle T., Gabici S., 2014, ApJ, 786, L24
Dunham M. M. et al., 2016, ApJ, 823, 160
Dunham M. M., Arce H. G., Mardones D., Lee J.-E., Matthews B. C., Stutz A. M., Williams J. P., 2014, ApJ, 783, 29
Ferrand G., Safi-Harb S., 2012, Adv. Space Res., 49, 1313
Flower D. R., Pineau des Forêts G., 2003, MNRAS, 343, 390
Governato F. et al., 2010, Nature, 463, 203
Green D. A., 2019, JA&A, 40, 36
Gusdorf A., Cabrit S., Flower D. R., Pineau Des Forêts G., 2008, A&A, 482, 809
Heckman T. M., Thompson T. A., 2017, Handbook of Supernovae, Springer International Publishing AG,p. 2431, preprint (arXiv:1701.09062)
Hennebelle P., Iffrig O., 2014, A&A, 570, A81

Hewitt J. W., Yusef-Zadeh F., Wardle M., Roberts D. A., Kassim N. E., 2006, ApJ, 652, 1288
Hopkins P. F., Kereš D., Oñorbe J., Faucher-Giguère C.-A., Quataert E., Murray N., Bullock J. S., 2014, MNRAS, 445, 581
Huang Y. L., Thaddeus P., 1986, ApJ, 309, 804
Iffrig O., Hennebelle P., 2015, A&A, 576, A95
Inutsuka S.-i., Inoue T., Iwasaki K., Hosokawa T., 2015, A&A, 580, A49
Issaoun S. et al., 2017, A&A, 606, A126
Jiménez-Serra I., Martín-Pintado J., Rodríguez-Franco A., Martín S., 2005, ApJ, 627, L121
Jiménez-Serra I., Caselli P., Martín-Pintado J., Hartquist T. W., 2008, A&A, 482, 549
Katz N., 1992, ApJ, 391, 502
Kim C.-G., Ostriker E. C., 2015, ApJ, 815, 67
Kimm T., Cen R., 2014, ApJ, 788, 121
Klessen R. S., Glover S. C. O., 2016, Saas Fee Adv. Course, 43, 85
Koeppen J., Kegel W. H., 1980, A&AS, 42, 59
Kokusho T., Torii H., Nagayama T., Kaneda H., Sano H., Ishihara D., Onaka T., 2020, ApJ, 899, 49
Koo B.-C., Kim C.-G., Park S., Ostriker E. C., 2020, ApJ, 905, 35
Körtgen B., Seifried D., Banerjee R., Vázquez-Semadeni E., Zamora-Avilés M., 2016, MNRAS, 459, 3460
Kruijssen J. M. D. et al., 2019, Nature, 569, 519
Krumholz M. R., Dekel A., McKee C. F., 2012, ApJ, 745, 69
Leitherer C. et al., 1999, ApJS, 123, 3
Leroy A. K. et al., 2013, AJ, 146, 19
Li M., Ostriker J. P., Cen R., Bryan G. L., Naab T., 2015, ApJ, 814, 4
Liu M., Tan J. C., Marvil J., Kong S., Rosero V., Caselli P., Cosentino G., 2020, ApJ, 921, 96
López-Sepulcre A. et al., 2011, A&A, 526, L2
López-Sepulcre A., Codella C., Cesaroni R., Marcelino N., Walmsley C. M., 2009, A&A, 499, 811
Marinacci F., Sales L. V., Vogelsberger M., Torrey P., Springel V., 2019, MNRAS, 489, 4233
Martin-Pintado J., Bachiller R., Fuente A., 1992, A&A, 254, 315
Martizzi D., Faucher-Giguère C.-A., Quataert E., 2015, MNRAS, 450, 504
Martizzi D., Fielding D., Faucher-Giguère C.-A., Quataert E., 2016, MNRAS, 459, 2311
Neufeld D. A., Hollenbach D. J., Kaufman M. J., Snell R. L., Melnick G. J., Bergin E. A., Sonnentrucker P., 2007, ApJ, 664, 890
Noriega-Crespo A., Moro-Martin A., Carey S., Morris P. W., Padgett D. L., Latter W. B., Muzerolle J., 2004, ApJS, 154, 402
Padoan P., Pan L., Haugbølle T., Nordlund, Å., 2016, ApJ, 822, 11
Padoan P., Haugbølle T., Nordlund, Å., Frimann S., 2017, ApJ, 840, 48
Parmentier G., 2011, MNRAS, 413, 1899
Petre R., Szymkowiak A. E., Seward F. D., Willingale R., 1988, ApJ, 335, 215
Reach W. T., Tram L. N., Richter M., Gusdorf A., DeWitt C., 2019, ApJ, 884, 81
Rho J., Petre R., 1998, ApJ, 503, L167
Sanderson R. E. et al., 2018, ApJ, 869, 12
Scannapieco C., Tissera P. B., White S. D. M., Springel V., 2008, MNRAS, 389, 1137
Schilke P., Walmsley C. M., Pineau des Forets G., Flower D. R., 1997, A&A, 321, 293
Sedov L. I., 1959, Similarity and Dimensional Methods in Mechanics. Academic Press, New York
Seifried D., Haid S., Walch S., Borchert E. M. A., Bisbas T. G., 2020, MNRAS, 492, 1465
Shima K., Tasker E. J., Habe A., 2017, MNRAS, 467, 512
Slane P., Bykov A., Ellison D. C., Dubner G., Castro D., 2016, Multi-scale Structure Formation and Dynamics in Cosmic Plasmas, Space Sciences Series of ISSI, Vol. 51. Springer Science+Business Media, New York, p. 187
Smith M. C., Sijacki D., Shen S., 2018, MNRAS, 478, 302
Sobolev V. V., 1957, Soviet Ast., 1, 678
Stephens I. W. et al., 2017, ApJ, 846, 16
Stinson G., Seth A., Katz N., Wadsley J., Governato F., Quinn T., 2006, MNRAS, 373, 1074
Taylor G., 1950, Proc. R. Soc. London Ser. A, 201, 159
Teyssier R., Pontzen A., Dubois Y., Read J. I., 2013, MNRAS, 429, 3068
Troja E., Bocchino F., Reale F., 2006, ApJ, 649, 258
Troja E., Bocchino F., Miceli M., Reale F., 2008, A&A, 485, 777
Ustamujic S., Orlando S., Greco E., Miceli M., Bocchino F., Tutone A., Peres G., 2021, A&A, 649, A14
van der Tak F. F. S., Black J. H., Schöier F. L., Jansen D. J., van Dishoeck E. F., 2007, A&A, 468, 627
van Dishoeck E. F., Jansen D. J., Phillips T. G., 1993, A&A, 279, 541
Vasyunina T., Linz H., Henning T., Zinchenko I., Beuther H., Voronkov M., 2011, A&A, 527, A88
Vaupre S., 2015, PhD thesis, University of Grenoble
Verheyen L., Messineo M., Menten K. M., 2012, A&A, 541, A36
Wetzel A. R., Hopkins P. F., Kim J.-h., Faucher-Giguère C.-A., Kereš D., Quataert E., 2016, ApJ, 827, L23
White G. J., Rainey R., Hayashi S. S., Kaifu N., 1987, A&A, 173, 337
Wootten H. A., 1977, ApJ, 216, 440
Wright E. L. et al., 2010, AJ, 140, 1868
Zeng S. et al., 2017, A&A, 603, A22
Zhang D., Chevalier R. A., 2019, MNRAS, 482, 1602
Zhang Q., Hunter T. R., Brand J., Sridharan T. K., Cesaroni R., Molinari S., Wang J., Kramer M., 2005, ApJ, 625, 864
Zhang Z., Gao Y., Wang J., 2010, Sci. China Phys. Mech. Astron., 53, 1357
Ziurys L. M., Snell R. L., Dickman R. L., 1989, ApJ, 341, 857

This paper has been typeset from a TEX/LATEX file prepared by the author.